Dicke-model simulation via cavity-assisted Raman transitions

Zhiqiang Zhang,[1,*] Chern Hui Lee,[1] Ravi Kumar,[1] K. J. Arnold,[1] Stuart J. Masson,[2] A. L. Grimsmo,[3] A. S. Parkins,[2] and M. D. Barrett[1,4]

[1]*Centre for Quantum Technologies, 3 Science Drive 2, 117543 Singapore*

[2]*Dodd-Walls Centre for Photonics and Quantum Technologies, Department of Physics, University of Auckland, Private Bag 92019, Auckland, New Zealand*

[3]*ARC Centre of Excellence for Engineered Quantum Systems, School of Physics, The University of Sydney, Sydney, New South Wales 2006, Australia*

[4]*Department of Physics, National University of Singapore, 2 Science Drive 3, 117551 Singapore*

(Received 29 January 2018; published 25 April 2018)

The Dicke model is of fundamental importance in quantum mechanics for understanding the collective behavior of atoms coupled to a single electromagnetic mode. Here, we demonstrate a Dicke-model simulation via cavity-assisted Raman transitions in a configuration using counterpropagating laser beams. The observations indicate that motional effects should be included to fully account for the results. These results are contrary to experiments using single-beam and copropagating configurations. We give a theoretical description that accounts for the beam geometries used in the experiments and indicates the potential role of motional effects. In particular, a model is given that highlights the influence of Doppler broadening on the observed phase-transition thresholds.

DOI: 10.1103/PhysRevA.97.043858

I. INTRODUCTION

The Dicke model describes an ensemble of N two-level atoms coupled to a single electromagnetic mode [1,2], of which the phase transitions to superradiant and oscillatory states are fascinating [3–6]. It provides an active avenue of research in cavity quantum electrodynamics (QED) [6–10], and circuit QED [11–15]. Since the original Dicke model was introduced [1], much theoretical progress has been made, for example, description of thermodynamic properties [4,16–18], chaos [19], finite-size scaling [20,21], nonequilibrium and dissipation [5,8,22–30], spin glasses [31], and spin squeezing [32,33].

Experimental realizations of the Dicke model have utilized Bose-Einstein condensate (BEC) [7,34–38], superconducting qubits coupled to resonators [15], or cavity-assisted Raman transitions with cold atoms [6,39]. The latter [39], which was based on a scheme derived from the proposal in [2], offers the advantage that all parameters of the Dicke model are independently tuneable. Our implementation here provides additional benefits compared to [39]: (i) allowing more independent control of both the coupling beams, and (ii) providing real-time control of the atom number based on nondestructive measurements of the cavity dispersion enabled by a field-programmable gate array (FPGA). These improvements result in cleaner data collection which reduces dependence on post-selection. Our implementation has also enabled us to explore the nonequilibrium phase transitions using an implementation based on a collection of spin-1 atoms [6].

In this work, we give a detailed account of a Dicke-model simulation using cavity-assisted Raman transitions along with a discussion of relevant theory, which follows the original proposal in [2] but allows for more general beam geometries as used in the experiments. The beam geometry has a significant influence on the potential effects of motion and the validity of a Dicke-model simulation. Counter- and copropagating beam geometries are demonstrated experimentally and the results are contrasted with that of a single-beam configuration. Observed thresholds agree with theoretical predictions that includes the influence of Doppler broadening. This work provides useful information for understanding the interaction of light and an atomic ensemble coupled to a single electromagnetic mode.

II. EXPERIMENTAL SETUP

The experimental setup is similar to the one described elsewhere [6,40]. An ensemble of ^{87}Rb atoms is trapped within an optical cavity using an intracavity 1560 nm optical lattice. The cavity is detuned from the $^2S_{1/2}$ to $^2P_{3/2}$ transition by $\Delta = -2\pi \times 127$ GHz. Relative to this transition, the cavity parameters are $(g,\kappa,\gamma_a) = 2\pi \times (1.1,0.1,3)$ MHz, where g is the single-atom-cavity coupling constant for the $|F = 2, m_F = 2\rangle$ to $|F' = 3, m_{F'} = 3\rangle$ cycling transition; κ and γ_a are the half-width at half-maximum linewidth of the cavity and the atomic dipole decay rate, respectively. The wavelength of the 1560 nm optical lattice is exactly twice the cavity resonance near the $^2S_{1/2}$ to $^2P_{3/2}$ transition, thus the atoms are trapped very close to alternate antinodes of the cavity field, maximizing the atom-cavity coupling. The atoms are driven transverse to the cavity by two laser beams which are approximately equal in power. As with the cavity coupling, the coupling strengths Ω_s and Ω_r are for the $|F = 2, m_F = 2\rangle$ to $|F' = 3, m_{F'} = 3\rangle$ cycling transition. Each beam drives a cavity-assisted Raman transition between the two hyperfine ground states, as depicted in Fig. 1. The beams are linearly polarized with a polarization

*e0000155@u.nus.edu

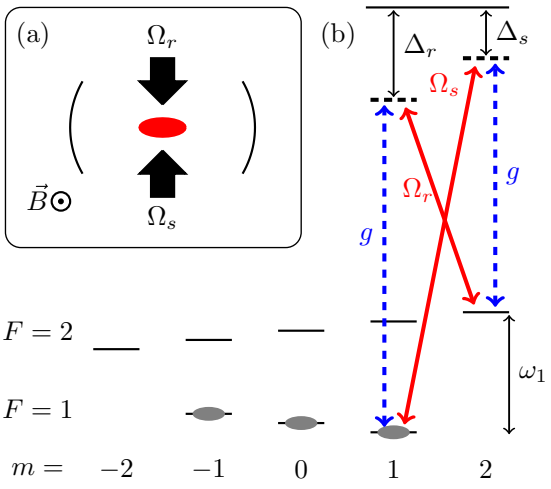

FIG. 1. (a) Schematic representation of the counterpropagating probe beam geometry, and (b) atomic level structure for Dicke-model implementation. Red lines are classical beam couplings and dashed blues lines are cavity-mode couplings. The frequency ω_1 is the separation of the two states relevant to the Dicke model inclusive of the ground-state hyperfine splitting and Zeeman shifts. Note that as defined in the text, the detunings Δ_r and Δ_s would have negative values, as drawn in the figure.

orthogonal to a magnetic field that defines the quantization axis. The cavity output is detected using either a single-photon counting module (SPCM) for maximum sensitivity or optical hetrodyne detection for a larger dynamic range.

III. THEORY

Derivation of the Hamiltonian follows the treatment given in [2] while retaining the phases of the driving fields. After adiabatic elimination of the excited states, the Hamiltonian for the experimental setup shown in Fig. 1 is given by

$$H = \omega\, a^\dagger a + \omega_0\, J_z + \frac{\delta}{N} a^\dagger a\, J_z + H_R, \tag{1}$$

where

$$H_R = \frac{\sqrt{3}}{12\Delta_r}\sum_{j=1}^{N}[g(\mathbf{r}_j)\,\Omega_r\, e^{-i(\mathbf{k}_r\cdot\mathbf{r}_j+\theta_r)} a J_{+,j} + \text{H.c.}] + \frac{\sqrt{3}}{12\Delta_s}\sum_{j=1}^{N}[g(\mathbf{r}_j)\,\Omega_s\, e^{i(\mathbf{k}_s\cdot\mathbf{r}_j+\theta_s)} a^\dagger J_{+,j} + \text{H.c.}], \tag{2}$$

$$\omega_0 = \omega_1 - \frac{1}{2}(\omega_s - \omega_r) + \frac{1}{6}\left\{\left(\frac{\Omega_r^2}{\Delta_r} - \frac{\Omega_r^2}{\Delta_r - \omega_1}\right) - \left(\frac{\Omega_s^2}{\Delta_s} - \frac{\Omega_s^2}{\Delta_s + \omega_1}\right)\right\}, \tag{3}$$

$$\omega = \omega_c - \frac{1}{2}(\omega_r + \omega_s) + \frac{N}{3}\left(\frac{\langle g^2\rangle}{\Delta_s} + \frac{\langle g^2\rangle}{\Delta_r}\right), \tag{4}$$

and

$$\delta = \frac{2N}{3}\left(\frac{\langle g^2\rangle}{\Delta_s} - \frac{\langle g^2\rangle}{\Delta_r}\right). \tag{5}$$

In these expressions, $\langle\cdot\rangle$ is an average over the spatial distribution of atoms and ω_1 is the Zeeman-shifted hyperfine splitting between the states of interest. With the definitions

$$|0\rangle \equiv |F = 1, m_F = 1\rangle, \tag{6}$$

$$|1\rangle \equiv |F = 2, m_F = 2\rangle, \tag{7}$$

the single-particle angular momentum operators $J_{\pm,j}$ and $J_{z,j}$ are defined by

$$J_{+,j} = |1_j\rangle\langle 0_j|, \quad J_{-,j} = |0_j\rangle\langle 1_j|, \tag{8}$$

and

$$J_{z,j} = \tfrac{1}{2}(|1_j\rangle\langle 1_j| - |0_j\rangle\langle 0_j|), \tag{9}$$

with collective counterparts

$$J_\pm = \sum_j J_{\pm,j}, \quad J_z = \sum_j J_{z,j}. \tag{10}$$

For a suitable choice of $\theta_{r,s}$, $\Omega_{r,s}$ can be assumed real. However, the dependence on θ_r and θ_s can be removed using the unitary transform

$$U_\theta = \exp\left(i\frac{\theta_r - \theta_s}{2} J_z\right)\exp\left(-i\frac{\theta_r + \theta_s}{2} a^\dagger a\right), \tag{11}$$

assuming these do not have significant temporal variation over the timescale of an experiment.

As the atoms are confined at alternate antinodes of the cavity mode, $g(\mathbf{r}_j)$ is approximately constant and we approximate it by its thermally averaged value, $\langle g\rangle$. For counterpropagating beams, $\mathbf{k}_r \approx -\mathbf{k}_s \equiv \mathbf{k}$ and the phase terms $e^{\pm i\mathbf{k}\cdot\mathbf{r}_j}$ can be removed from H_R using the unitary transformation

$$U_\mathbf{k} = \prod_j \exp[i(\mathbf{k}\cdot\mathbf{r}_j)J_{z,j}]. \tag{12}$$

This then leads to the Hamiltonian

$$H = \omega a^\dagger a + \omega_0 J_z + \frac{\delta}{N} a^\dagger a J_z + \frac{\lambda_r}{\sqrt{N}}(a J_+ + a^\dagger J_-) + \frac{\lambda_s}{\sqrt{N}}(a J_- + a^\dagger J_+) + H_1, \tag{13}$$

where

$$\lambda_r = \frac{\sqrt{3N}}{12}\frac{\Omega_r\langle g\rangle}{\Delta_r}, \quad \lambda_s = \frac{\sqrt{3N}}{12}\frac{\Omega_s\langle g\rangle}{\Delta_s}. \tag{14}$$

In carrying out this last unitary transformation, we have treated the positions as fixed numbers, which effectively ignores motional effects. Including the motion adds a term,

$$H_1 = \omega_T \sum_j b_j^\dagger b_j + \sum_j (\mathbf{k}\cdot\mathbf{v}_j) J_{z,j}, \tag{15}$$

to the Hamiltonian, where ω_T denotes the trap frequency associated with the harmonic confinement along the propagation direction of the lasers, and b_j is the associated ladder operator for the jth atom. The last term in the expression for H_1 arises from the transformation given in Eq. (12) and it reflects the sensitivity of ω_0 to Doppler shifts in the counterpropagating configuration. Interpretation as a simple, idealized Dicke

model thus implicitly neglects motional effects and requires the classical beams to be counterpropagating.

The parameters ω and ω_0 are specified in terms of the mean and difference of the laser frequencies, which can be conveniently referenced, respectively, to the cavity resonance and the hyperfine splitting between the two states of interest. They can equally be expressed in terms of the detuning of each beam from the Raman resonance with the cavity. For this purpose, we define

$$\omega_{\rm d} = \frac{N}{3}\left(\frac{\langle g^2\rangle}{\Delta_{\rm s}} + \frac{\langle g^2\rangle}{\Delta_{\rm r}}\right) \tag{16}$$

and

$$\Delta\omega_{\rm ss} = \frac{1}{6}\left\{\left(\frac{\Omega_{\rm r}^2}{\Delta_{\rm r}} - \frac{\Omega_{\rm r}^2}{\Delta_{\rm r}-\omega_1}\right) - \left(\frac{\Omega_{\rm s}^2}{\Delta_{\rm s}} - \frac{\Omega_{\rm s}^2}{\Delta_{\rm s}+\omega_1}\right)\right\}, \tag{17}$$

and we may write

$$\delta_{\rm cr} \equiv \omega_0 - \omega = \omega_{\rm r} - \omega_c + \omega_1 - \omega_{\rm d} + \Delta\omega_{\rm ss}, \tag{18a}$$

$$\delta_{\rm cs} \equiv -(\omega_0 + \omega) = \omega_{\rm s} - \omega_c - \omega_1 - \omega_{\rm d} - \Delta\omega_{\rm ss}. \tag{18b}$$

In the limit that $\delta = 0$, these are simply the detunings of each beam from Raman resonance with the cavity, properly accounting for cavity dispersion and ac Stark shifts. For $\delta \neq 0$, the detunings from Raman resonance become a dynamical quantity as the population moves from one state to the other.

Since $|\Delta_{\rm r,s}| \gg \omega_1$, it is convenient to write $\Delta_{\rm r} = \Delta - \omega_1/2$ and $\Delta_{\rm s} = \Delta + \omega_1/2$. Then, taking $\Omega_{\rm r} \approx \Omega_{\rm s} = \Omega$, we have

$$\omega_{\rm d} = \frac{2}{3}\frac{N\langle g^2\rangle}{\Delta}, \quad \delta = -\omega_{\rm d}\frac{\omega_1}{\Delta}, \quad \Delta\omega_{\rm ss} = -\frac{1}{3}\frac{\Omega^2}{\Delta^2}\omega_1, \tag{19}$$

correct to first order in ω_1/Δ. In all cases, N represents the number of atoms within the two-level system of interest. Atoms outside this subspace simply add an additional dispersive shift in the definition of ω.

IV. EXPERIMENTAL IMPLEMENTATION

An experiment starts by preparing a set number of atoms in the $F = 1$ ground-state manifold with a well-defined temperature, which is achieved as follows. First, a magneto-optical trap (MOT) is formed 15 mm above the cavity. The atoms are then pumped into the $F = 1$ hyperfine manifold and transferred to a single-beam 1064 nm dipole trap that is overlapped with the MOT. Typically, around 5×10^6, atoms are loaded into the dipole trap. Using a motorized translation stage, the beam is then moved down 15 mm over one second to bring the atoms into the cavity. The power of the 1064 nm beam is then adiabatically lowered in 350 ms to transfer the atoms into the 1560 nm intracavity optical lattice with a predefined depth. The number of atoms transferred to the intracavity optical lattice is determined nondestructively by measuring the dispersive shift, $\omega_{\rm d}$, of the cavity by sweeping the frequency of a weak probe beam over the cavity resonance in 3 ms and recording the cavity transmission.

A fixed atom number is maintained run to run using an FPGA which triggers the experiment once a set value is reached. Explicitly, the cavity probe beam is set to a fixed frequency slightly less than the maximum dispersive shift. We then monitor the cavity transmission using the SPCM and record the count rate with the FPGA. As the atoms are lost due to background collisions, the cavity is moved into resonance with the probe beam, increasing the output photon count rate. When the count rate reaches a preset threshold, the FPGA is triggered and clocks out the rest of the programmed experiment time sequence. Strictly speaking, it is the dispersive shift that is fixed, and the accuracy of the atom number is limited by spatial averaging over the thermal distribution of atoms. This procedure provides a high degree of repeatability in the experiment with evaporation ensuring a well-defined temperature relative to the depth of the intracavity 1560 nm optical lattice, and triggering off a set dispersive shift then fixes a well-defined atom number. Remaining variation in the dispersive shift can be further reduced by postselection, as it is also measured *in situ* both immediately after the FPGA has been triggered and after the experiment is completed.

In the experiment, all lasers are referenced to a high-finesse transfer cavity with a linewidth of ~50 kHz at both 780 and 1560 nm. In addition, the experiment cavity is locked to the 1560 nm laser. This allows all laser detunings to be accurately set relative to the empty experiment cavity resonance at 780 nm. The two laser fields in Fig. 1 are obtained from a single laser using sidebands generated from a wideband electro-optic modulator (EOM). Hence, $(\omega_{\rm s} - \omega_{\rm r})/2$ is set by the driving frequency of the EOM and $\omega_c - (\omega_{\rm r} + \omega_{\rm s})/2$ is the detuning of the carrier with respect to the empty cavity. Complete specification of the model parameters then requires a measurement of ω_1 and a characterization of $\lambda_{\rm r,s}$ in addition to the *in situ* measurement of the dispersive shift.

To characterize the coupling strengths $\lambda_{\rm r,s}$ as a function of power, we note that when $\lambda_{\rm s} = 0$, the Hamiltonian reduces to a Tavis-Cummings interaction. Weak probing of the cavity then provides an avoided crossing with a splitting that is determined by $\lambda_{\rm r}$. Fitting the cavity transmission as a function of both the probe detuning with respect to the cavity and the cavity detuning with respect to the Raman resonance then allows us to extract both the coupling strength $\lambda_{\rm r}$ and the splitting ω_1. The splitting is shifted by the differential ac Stark shift from the coupling beam, but this can be inferred from the measured dispersive shift $\omega_{\rm d}$, the measured value of $\lambda_{\rm r}$, and by accounting for thermal averaging.

V. DICKE-MODEL THRESHOLD

With the model parameters fully characterized, we can explore the expected threshold behavior. As λ is increased, a phase transition occurs at a threshold given by [2],

$$\lambda_c = \frac{1}{2}\sqrt{\frac{\omega_0}{\omega}(\omega^2 + \kappa^2)}. \tag{20}$$

This equation does not include the effect of δ or decoherence. A small, nonzero δ simply displaces the value of ω and decoherence can be accounted for by considering a decay rate γ of the collective spin [25,29,30]. The result is the more general expression

$$\lambda_c = \frac{1}{2}\sqrt{\frac{\omega_0^2 + \gamma^2}{-2\langle\sigma_{\rm z}\rangle\omega_0}\frac{(\omega - \delta/2)^2 + \kappa^2}{\omega - \delta/2}}, \tag{21}$$

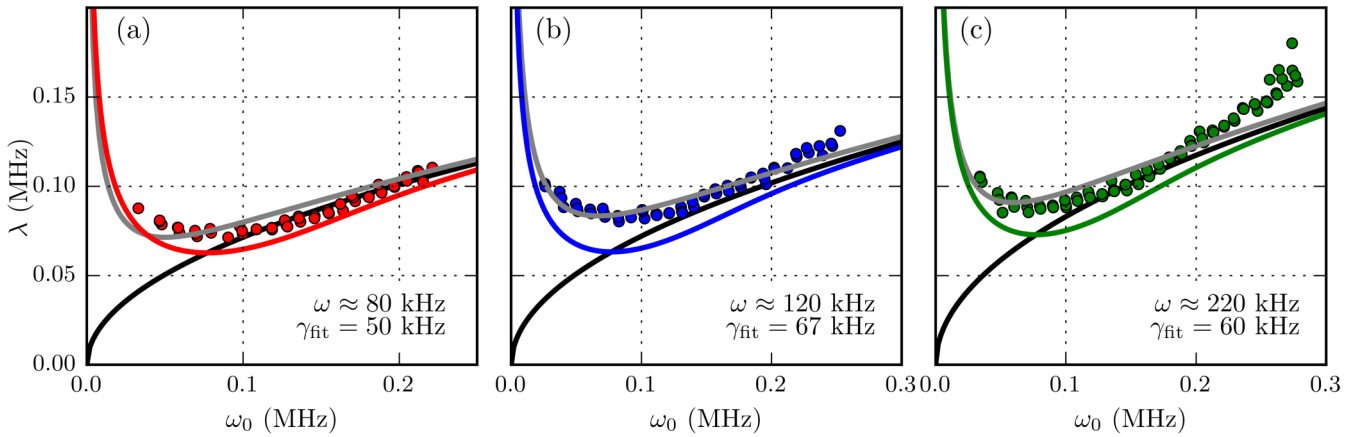

FIG. 2. Measured critical coupling as a function of ω_0 for selected fixed values of ω. The solid black lines are an *ab initio* calculation of the threshold from Eq. (20). Gray curves are fit to the experimental data using Eq. (21) with $\langle\sigma_z\rangle = -0.5$ and γ as a free parameter. For experimental data, the trap depth is fixed at 219 μK. Considering the equivalent rms Doppler broadening of $\gamma_d = 2\pi \times 59$ kHz, colored solid curves are obtained using Eq. (22).

where $\langle\sigma_z\rangle$ is the expectation value of the initial spin normalized by the number of atoms and accounts for imperfect initial-state preparation.

As discussed in the Appendix, inhomogeneous broadening arising from the velocity distribution of the atoms can also modify the threshold in a manner qualitatively similar to Eq. (21). Consideration of inhomogeneous broadening results in the threshold

$$\lambda_c = \sqrt{\frac{\sqrt{2}\gamma_d[(\omega-\delta/2)^2+\kappa^2]}{8(\omega-\delta/2)F\left(\frac{\omega_0}{\sqrt{2}\gamma_d}\right)}}, \tag{22}$$

where $F(x)$ is the Dawson function and γ_d is the root mean-square (rms) Doppler shift. This equation reduces to Eq. (21) in the limit $(\gamma_d, \gamma, \langle\sigma_z\rangle) \to (0, 0, -0.5)$.

To determine the threshold experimentally, a fixed number of atoms is prepared in the $F = 1$ level, as described in the previous section. For each run, after the FPGA trigger and *in situ* dispersive shift measurement, the laser fields are switched on at low power and then ramped over 3 ms to a final maximum power, while monitoring the output from the cavity using an SPCM. The threshold is inferred from the point of the ramp at which the photon count reaches a preset value (10 counts/5 μs, to be well above the background).

Figures 2 and 3 show the measured threshold as a function of ω_0 for fixed values of ω. For each graph, we give a curve (black) given by Eq. (20), a fit (gray) to Eq. (21) using γ as the fitting parameter, and a theoretical plot (red, blue, or green color plot) accounting for the effects of inhomogeneous broadening as given by Eq. (22). In the experiment, two obvious mechanisms for decoherence are spontaneous emission and collisions. Spontaneous-emission rates are proportional to λ^2 [6] and we estimate values of a few hundred per second over the range of experimental values explored. These are too small to account for the fitted values of γ as is the collision rate which is estimated to be ~ 1000/s for Fig. 2 and ~ 400/s for Fig. 3. Alternatively, Doppler shifts appearing in Eq. (15) can be expected to play a role, particularly for smaller values of ω_0. For the data in Figs. 2 and 3, we estimate rms Doppler shifts of $\gamma_d = 2\pi \times 59{,}22$ kHz respectively. The model used to derive Eq. (22) explicitly includes Doppler shifts arising from the motion of the atoms and captures the qualitative behavior of the observed thresholds.

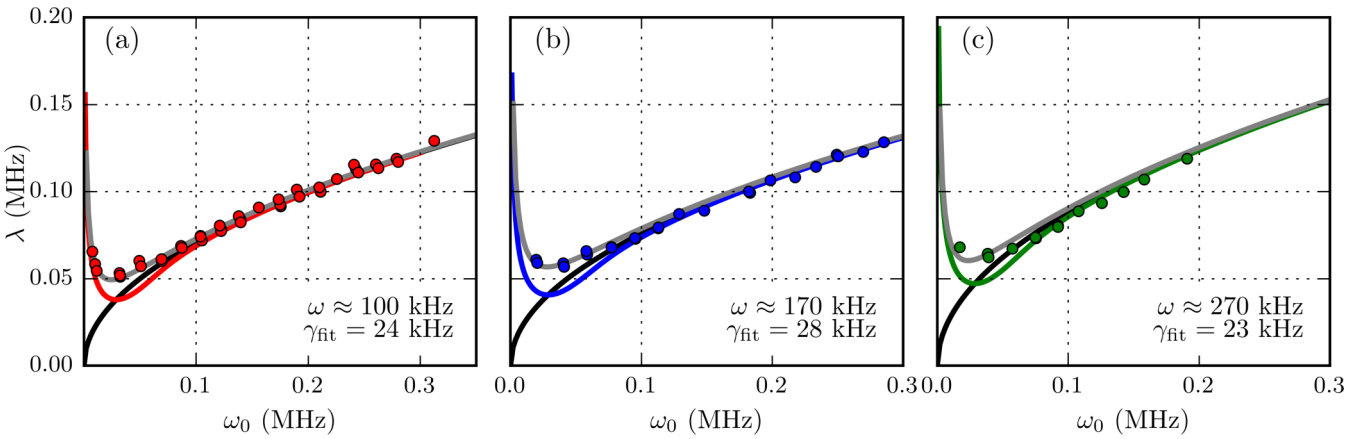

FIG. 3. Same as Fig. 2, except with trap depth fixed at 31 μK, with the equivalent rms Doppler broadening of $2\pi \times 22$ kHz.

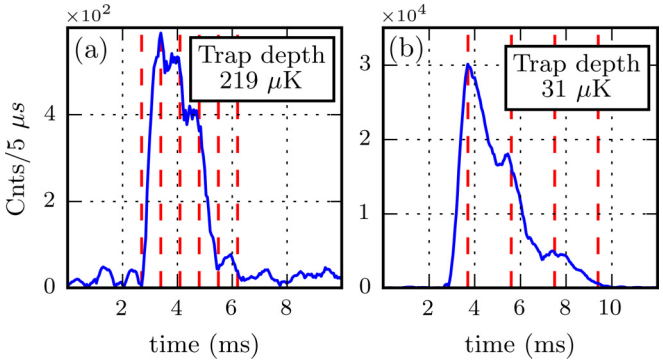

FIG. 4. Typical cavity outputs observed using heterodyne detection. The parameters $\omega = 2\pi \times 100$ kHz and $\omega_0 = 2\pi \times 215$ kHz for both (a) and (b). The trap depths are fixed at (a) 219 μK and (b) 31 μK. The red dashed lines are spaced at $T/2$, where T is the period of harmonic oscillation in the direction of the probe laser for the respective trap depths.

Trap depth also has a pronounced effect on output intensity from the cavity during the superradiant phase. In Figs. 4(a) and 4(b), typical output signals are presented for the trap depths of 219 and 31 μK, respectively. These signals are derived from a heterodyne detection setup in order to avoid saturation of the SPCM. Aside from the overall scale of the output signal, it is worth noting the output duration. When including a decay mechanism for the collective spin, the resulting semiclassical equations predict a finite pulse duration with a timescale given by $1/\gamma$. For the outputs shown in Fig. 4, this timescale is more consistent with those associated with the spontaneous emission and collisions than with the values of γ, inferred by fitting the threshold data to Eq. (21), or γ_d. This suggests that the Doppler broadening is an important factor in reaching the transition but less so in the subsequent dynamics. However, apparent in the outputs are marked plateaus. The vertical lines given in the plots are separated by half the period of oscillation associated with motion in the direction of the probe. This suggests that periodic motion of the atoms may play a role in the dynamics beyond the phase transition.

The experimental implementation allows both positive and negative values of ω and ω_0. Figure 5 shows the obtained threshold with ω varying over both positive and negative values for a fixed positive value of $\omega_0 > 0$ [41]. Changing the

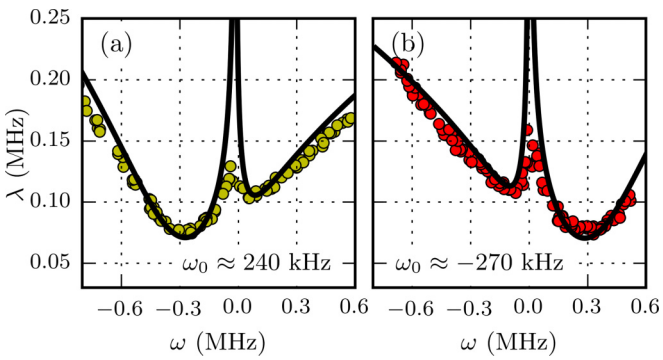

FIG. 5. Measured critical coupling as function of ω for (a) $\omega_0 > 0$ and (b) $\omega_0 < 0$. Solid black lines show the critical coupling strength calculated *ab initio* from the theory given in the Appendix.

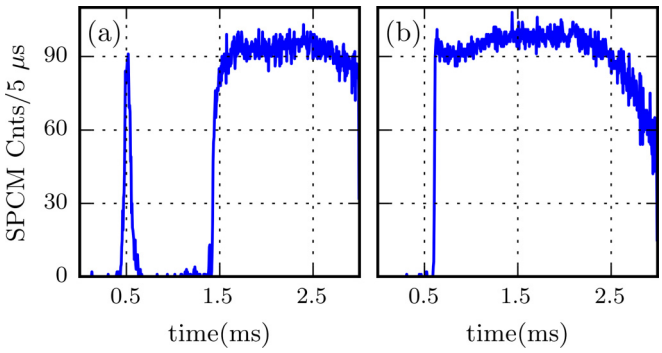

FIG. 6. Typical cavity output pulses in the parameter regimes, (a) $\omega\omega_0 < 0$ and (b) $\omega\omega_0 > 0$.

sign of both ω and ω_0 amounts to changing the sign of both laser detunings from their respective cavity-assisted Raman resonances and is of no physical consequence. The relative sign of ω and ω_0, however, determines the interpretation of the initial state with the atoms pumped to $F = 1$. When ω and ω_0 have the same sign, the initial state is given by $|N/2, -N/2\rangle$, which is a stable ground state of the Dicke-Hamiltonian below threshold. When ω and ω_0 have opposite signs, the initial state corresponds to $|N/2, N/2\rangle$. This can be understood by considering a unitary transformation $U = \exp(-i\pi J_y)$ corresponding to a rotation about the y axis by π. The transformation effectively flips the sign of ω_0 in the Hamiltonian and the eigenvalue of J_z for the initial state.

The relative sign of ω and ω_0 or, equivalently, the initial state has a clear signature in the output of the cavity, as shown in Fig. 6, representing typical cavity outputs corresponding to (a) $\omega > 0$ and (b) $\omega < 0$, respectively, for the threshold measurements shown in Fig. 5. When starting in the proper stable state of the Dicke model, that is $\omega > 0$, the cavity output is characterized by a single pulse as expected. When starting in the unstable state, the expected cavity output is preceded by a smaller, much shorter pulse, as in Fig. 6(a). We interpret this short pulse as a single-beam effect in which the atoms are transferred from the unstable state to the other. In this case, the threshold given in Fig. 5 is based on the appearance of the first pulse. However, we can define two such thresholds: one for the first pulse and one for the second. In Fig. 7, we

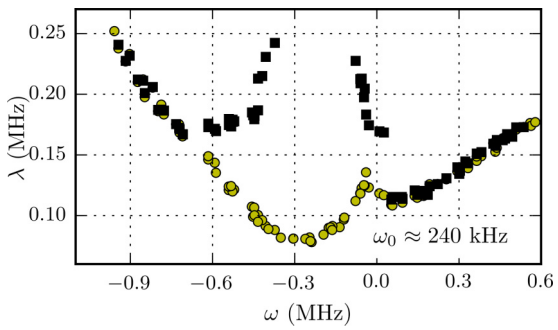

FIG. 7. The yellow dots are the same as shown in Fig. 5(a), where the threshold is determined from the first onset of light output from the cavity. The black squares are the thresholds extracted from the same data but neglecting the initial transient pulse, such as shown in Fig. 6(a), if one occurs.

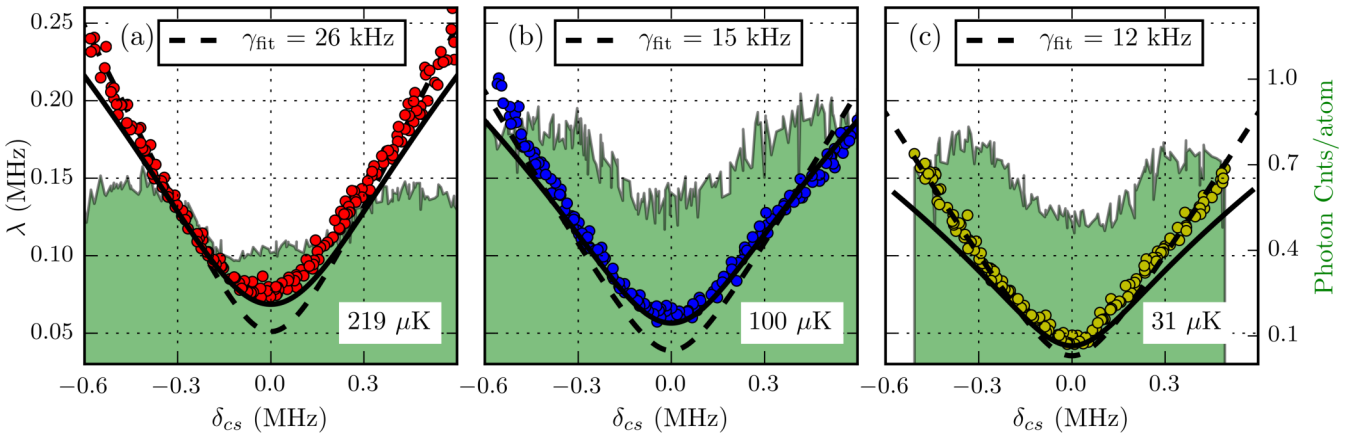

FIG. 8. Threshold for cavity output pulse for a single beam as a function of detuning from the cavity-assisted Raman resonance. Data is shown for three different traps depths: (a) 219 μK, (b) 100 μK, and (c) 31 μK, respectively. Black dashed curves are fits to the experiment data points, but only for $|\delta_{\rm cs}| > 250$ kHz using Eq. (23) with γ as a free parameter. The rms Doppler broadening due to thermal motion for the respective plots is estimated to be $2\pi \times [59,40,22]$ kHz. Black curves are obtained considering only the corresponding inhomogeneous broadenings, as discussed in the Appendix, using the experimentally determined Doppler broadening.

give an analysis showing the two thresholds with the data points in black obviously showing the threshold for the second pulse. Ideally, the first pulse would perfectly transfer the atoms from one state to the other, which would provide a more symmetric plot as expected from theory. The lack of symmetry indicates this is not the case. Additionally, as $|\omega|$ increases, the two pulses appear closer together and eventually coalesce. This is because the Dicke-model threshold eventually becomes smaller than the single-beam threshold, as shown in Fig. 9. Note that the theoretical model given in the Appendix correctly captures the threshold behavior across the entire parameter regime.

VI. SINGLE-BEAM THRESHOLD

Given the interpretation of the short duration pulse before superradiance, it is of interest to explore the single-beam case. In Fig. 8, we plot the threshold for this transient pulse with a single beam as a function of $\delta_{\rm cs} = -(\omega_0 + \omega)$. For this case, a nonzero threshold occurs in the presence of decoherence [25], in which case there must be sufficient driving to overcome decay of the collective spin. The semiclassical equations can be used to determine a threshold and we obtain the expression

$$\lambda_{\rm single} \geqslant \sqrt{\frac{\gamma\kappa}{-2\langle\sigma_z\rangle}\left[1+\left(\frac{\delta_{\rm cs}}{\gamma+\kappa}\right)^2\right]}, \tag{23}$$

where $\langle\sigma_z\rangle$ is the initial value which accounts for the imperfect state preparation.

When fitting the above equation to the data, it is found that fits typically underestimate the threshold for larger values of $\delta_{\rm cs}$ and overestimate otherwise. If Doppler broadening were important, it would be reasonable to conjecture that it would be less so for larger values of $\delta_{\rm cs}$. Hence, in Fig. 8, fits are given which exclude the points for which $|\delta_{\rm cs}| \leqslant 250$ kHz. Constrained in this way, the fits are notably better for lower temperatures and hence lower Doppler broadening. Again, as in the Dicke-model case, the fitted decay rate is well above that expected from collisions and spontaneous emission, but notably diminishes with temperature. As shown in the Appendix, inhomogeneous Doppler broadening can also give rise to a nonzero threshold in the single-beam case. Thresholds derived from that theory using the experimentally determined Doppler broadening are also included in Fig. 8 and are seen to better explain the data, at least for small values of $|\delta_{\rm cs}|$.

It is also of interest to directly compare the single-beam case to the results of the previous section. To this end, we determine the Dicke-model threshold as a function of $\delta_{\rm cs}$ for the two cases in which ω_0 is fixed at around $\pm 2\pi \times 250$ kHz. In Fig. 9, we plot the thresholds for these two cases, along with the single-beam case. The overlap in the region between around $\pm 2\pi \times 250$ kHz is consistent with the previous interpretation that the first of the two pulses seen in this region is a single-beam effect.

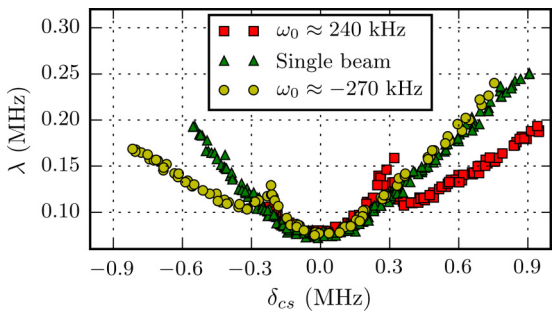

FIG. 9. Dicke-model threshold data from Fig. 5 (yellow dots and red squares) recast as a function of $\delta_{\rm cs}$ for direct comparison to the single-beam threshold data (green triangles).

VII. CAVITY-TRANSMISSION SPECTRUM

The improvement in stability and repeatability of the experiment has allowed us to verify the cavity-transmission spectrum near the critical coupling, as predicted in [2]. According to

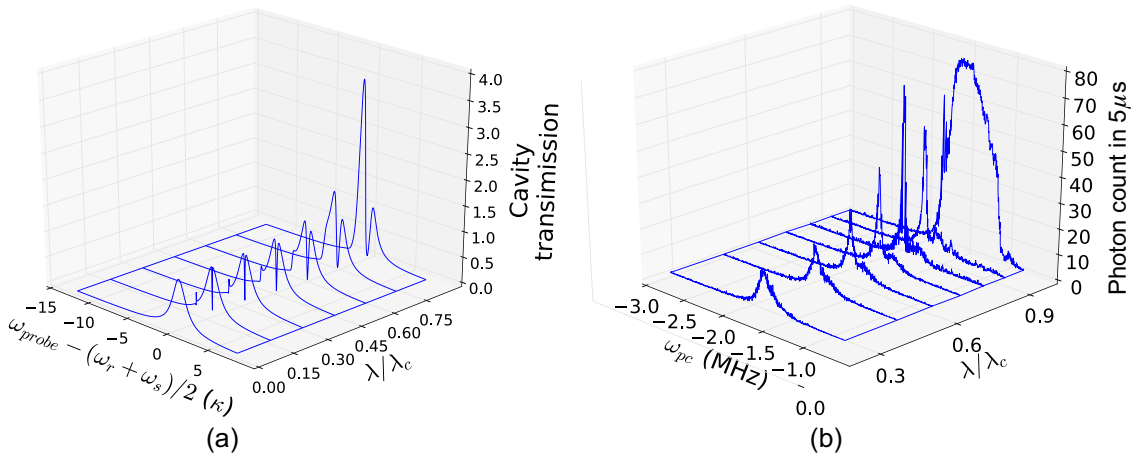

FIG. 10. (a) Theoretical transmission spectrum, calculated using the result of Ref. [2]. (b) Measured transmission spectrum for $\omega = 100$ kHz $= \omega_0$, and the dispersive shift $\omega_d = -1.7$ MHz. The threshold power is about 1.3 mW. Above the critical coupling, the detector is saturated by the superradiant pulse, as can be seen in the final trace, and the transmission spectrum cannot be measured using the SPCM.

Ref. [2], as the coupling strength is increased close to the critical coupling and the cavity is simultaneously probed with a weak classical beam, a peak is expected in the transmission at the average frequency of the two coupling lasers, $(\omega_s + \omega_r)/2$. To observe this, the power of the two coupling beams is first raised to a value close to the measured threshold. The transmission spectrum is then measured by sweeping the frequency of the cavity probe beam and measuring the output photons. The results are plotted in Fig. 10 along with the theoretical prediction. The larger peak in the measured transmission spectrum appears at smaller λ/λ_c compared to the theoretical prediction; this is possibly due to the fact that the cavity probe beam is not sufficiently weak as is assumed in the theoretical analysis. The intracavity field therefore brings λ above the critical coupling at a lower Raman beam power. This power of the cavity probe beam is, however, necessary to ensure a good signal-to-noise ratio in the transmission spectrum measurement.

VIII. COPROPAGATING VS COUNTERPROPAGATING

From Sec. III, it is clear that the copropagating case, as used in [39], does not support a simple Dicke-model interpretation. We have extensively reinvestigated this geometry over a wide range of parameters and, in most cases, the second beam plays no significant role. We illustrate this in Fig. 11(a), in which threshold data, as a function of the single-beam detuning δ_{cs}, is shown for both a single beam and copropagating beams with two different values of ω_0. This highlights the independence of ω_0 and hence the presence of the other beam.

The size of the observed cavity output pulse in the copropagating versus counterpropagating configuration further supports this conclusion. In the single-beam case, the complete population transfer of N atoms can generate, at most, N photons in the cavity. By integrating the total number of counts in the output pulse and accounting for the quantum efficiency of detecting an excitation in the cavity, we can estimate the average number of photons scattered per atom in the duration of the pulse. In all the data for the single-beam data and copropagating configuration (both from [39] and repeated experiments), the output pulse is typically short in duration ($\sim$100 μs) and the average number of photons scattered per atom is strictly <1, consistent with a (partial) population transfer in both cases.

As illustrated in Fig. 4(b), outputs in the counterpropagating configuration are sustained for several milliseconds with more than a hundred photons per atom scattered into the cavity. This strongly supports the conclusion that a quasistationary superradiant state consistent with the Dicke-model phase transition is observed in the counterpropagation configuration. The output

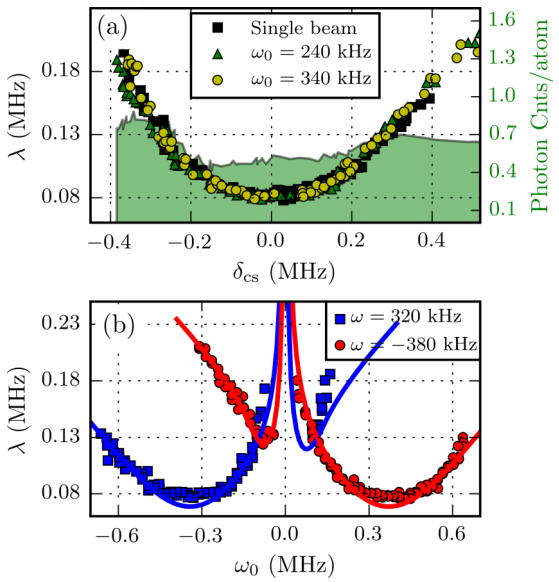

FIG. 11. (a) The experiment in the copropagating configuration with (green triangles) $\omega_0 = 2\pi \times 240$ kHz and (yellow dots) $\omega_0 = 2\pi \times 340$ kHz. Single-beam data is also shown for comparison. The solid green background is the average number of photons lost from the cavity per atom for the copropagating data run (green triangles). (b) Threshold in copropagating configuration as a function of ω_0 for two values of ω illustrating the narrow gap that occurs when $\omega_0 \approx 0$. Solid lines show the critical coupling strength calculated *ab initio* from the theory given in the Appendix.

pulses in the copropagating configuration, as observed in [39], on the other hand, are identical to those observed with only a single beam and thus do not support the conclusion of [39] that a Dicke-model simulation had been realized.

There is only one small parameter regime in which the second beam plays a significant role. This occurs when $\omega_0 \approx 0$ or, equivalently, when the laser detunings from their respective cavity-assisted Raman resonances are equal. The observed threshold as a function of ω_0 for a fixed value of $\omega = 2\pi \times 320$ kHz and $\omega = 2\pi \times -380$ kHz are given in Fig. 11(b), which clearly shows that the second beam effectively blocks the cavity-assisted Raman transfer when $\omega_0 \approx 0$. This phenomenon is adequately captured by the threshold model given in the Appendix, as illustrated by the solid curves given in Fig. 11(b).

IX. CONCLUSION

In this paper, we simulate a Dicke-model Hamiltonian using cold atoms with cavity-assisted Raman transitions. By implementing single-beam, copropagating, and counterpropagating beam configurations, we conclude that beam geometry is important for phase matching to realize a Dicke-model simulation. Experimental results show strong evidence of a Dicke-model realization in the case of a counterpropagating configuration. We develop a theoretical model that accounts for beam configuration as well as inhomogeneous broadening, and find reasonable agreement with experimental observations. It would be of interest to develop the theory further: to fully explore the consequences of motional coupling, its effects on the observed cavity outputs, and how the onset of superradiance influences the atomic motion.

ACKNOWLEDGMENTS

This research is supported by the National Research Foundation, Prime Ministers Office, Singapore and the Ministry of Education, Singapore under the Research Centres of Excellence programme (partly under Grant No. NRF-CRP12-2013-03). S.J.M. and A.S.P. acknowledge support from the Marsden Fund of the Royal Society of New Zealand (Contract No. UOA1328).

APPENDIX: INHOMOGENEOUS BROADENING EFFECTS

Here we consider the effects of inhomogeneous broadening on the observed thresholds in the single-beam and two-beam configurations. We assume the internal atomic and cavity dynamics are much faster than timescales governing external motion, and treat the position as a classical parameter. The Hamiltonian is then

$$H = \omega a^\dagger a + \omega_0 \sum_{j=1}^{N} \sigma_{z,j} + \frac{\lambda_r}{\sqrt{N}} \sum_{j=1}^{N} (e^{-i\phi_j} a \sigma_j^\dagger + e^{i\phi_j} a^\dagger \sigma_j) + \frac{\lambda_s}{\sqrt{N}} \sum_{j=1}^{N} (e^{\pm i\phi_j} a^\dagger \sigma_j^\dagger + e^{\mp i\phi_j} a \sigma_j), \tag{A1}$$

where the phases for each atom are given by $\phi_j = \mathbf{k} \cdot \mathbf{r}_j(t) = k r_j(t)$. The upper and lower signs in the last summation correspond to the co- and counterpropagating beam configurations, respectively. Since we are considering the threshold, we use the Holstein-Primakoff approximation $\sigma_j \approx b_j$, which is valid provided $b_j^\dagger b_j \ll 1$. The corresponding quantum Langevin equations are then

$$\dot{a} = -(\kappa + i\omega)a - \frac{i\lambda_r}{\sqrt{N}} \sum_v e^{ikr_j(t)} b_j - \frac{i\lambda_s}{\sqrt{N}} \sum_v e^{\pm ikr_j(t)} b_j^\dagger + \sqrt{2\kappa} a_{\text{in}}(t) \tag{A2}$$

and

$$\dot{b}_j = -i\omega_0 b_j - \frac{i\lambda_r}{\sqrt{N}} e^{-ikr_j(t)} a - \frac{i\lambda_s}{\sqrt{N}} \sum_v e^{\pm ikr_j(t)} a^\dagger. \tag{A3}$$

Substituting the formal solution

$$b_j(t) = e^{-i\omega_0 t} b_j(0) - \frac{i\lambda_r}{\sqrt{N}} \int_0^t e^{-ikr_j(t')} e^{-i\omega_0(t-t')} a(t') dt' - \frac{i\lambda_s}{\sqrt{N}} \int_0^t e^{\pm ikr_j(t')} e^{-i\omega_0(t-t')} a^\dagger(t') dt' \tag{A4}$$

into the equation for $\dot{a}$ gives

$$\begin{aligned} \dot{a} = &-(\kappa + i\omega)a - \frac{i\lambda_r}{\sqrt{N}} \sum_j e^{ikr_j(t)} e^{-i\omega_0 t} b_j(0) - \frac{i\lambda_s}{\sqrt{N}} \sum_j e^{\pm ikr_j(t)} e^{i\omega_0 t} b_j^\dagger(0) + \sqrt{2\kappa} a_{\text{in}}(t) \\ &- \frac{\lambda_r^2}{N} \left(\sum_j \int_0^t dt' e^{ik[r_j(t) - r_j(t')]} e^{-i\omega_0(t-t')} a(t') \right) + \frac{\lambda_s^2}{N} \left(\sum_j \int_0^t dt' e^{\pm ik[r_j(t) - r_j(t')]} e^{i\omega_0(t-t')} a(t') \right) \\ &- \frac{\lambda_r \lambda_s}{N} \sum_j \left(\int_0^t dt' e^{ik[r_j(t) \pm r_j(t')]} e^{-i\omega_0(t-t')} a^\dagger(t') - \int_0^t dt' e^{\pm ik[r_j(t) \pm r_j(t')]} e^{i\omega_0(t-t')} a^\dagger(t') \right). \end{aligned} \tag{A5}$$

Considering expectation values with $\langle b_v(0)\rangle = \langle b_v^\dagger(0)\rangle = \langle a_{\rm in}(t)\rangle = 0$ gives

$$\langle \dot a\rangle = -(\kappa + i\omega)a - \frac{\lambda_r^2}{N}\left(\sum_j \int_0^t dt' e^{ik[r_j(t)-r_j(t')]} e^{-i\omega_0(t-t')}\langle a(t')\rangle\right) + \frac{\lambda_s^2}{N}\left(\sum_j \int_0^t dt' e^{\pm ik[r_j(t)-r_j(t')]} e^{i\omega_0(t-t')}\langle a(t')\rangle\right)$$
$$- \frac{\lambda_r\lambda_s}{N}\sum_j\left(\int_0^t dt' e^{ik[r_j(t)\pm r_j(t')]} e^{-i\omega_0(t-t')}\langle a^\dagger(t')\rangle - \int_0^t dt' e^{\pm ik[r_j(t)\pm r_j(t')]} e^{i\omega_0(t-t')}\langle a^\dagger(t')\rangle\right). \tag{A6}$$

Note that only the cross terms proportional to $\lambda_r\lambda_s$ depend on the relative propagation direction of the beams. Since the cavity and atomic evolution is much faster than the external motion, we take $r_j(t) \approx r_j + v_j t$, where r_j and v_j are now to be considered initial conditions. In this case, the position dependence drops out of the first two integrals and is only relevant for the other two in the copropagating case. The summations can be approximated by integrals of the form

$$\frac{1}{N}\sum_j f(r_j, v_j) = \frac{1}{2\pi\bar v\sigma}\iint dv dr \exp\left(-\frac{r^2}{2\sigma^2}\right)\exp\left(-\frac{v^2}{2\bar v^2}\right) f(r,v), \tag{A7}$$

where $\bar v$ is the rms velocity and σ is the rms position. The cross terms do not contribute in the copropagating case since

$$\frac{1}{\sqrt{2\pi\sigma^2}}\int_{-\infty}^{\infty}\exp\left(-\frac{r^2}{2\sigma^2}\right)e^{2ikr}dr = e^{-2(k\sigma)^2} \approx 0, \tag{A8}$$

for distributions relevant to the experiments. Thus, in all cases, we are left with terms of the form

$$\frac{1}{\sqrt{2\pi\bar v^2}}\int_{-\infty}^{\infty}\int_0^t \exp\left(-\frac{v^2}{2\bar v^2}\right)e^{\pm i(\omega_0 - kv)(t-t')}\langle\mathcal{O}(t')\rangle dt' dv = \int_0^t \exp\left[-\frac{\gamma_{\rm d}^2(t-t')^2}{2}\right]e^{\pm i\omega_0(t-t')}\langle\mathcal{O}(t')\rangle dt', \tag{A9}$$

where $\gamma_{\rm d} = k\bar v$. The Laplace transform then gives

$$\int_0^\infty e^{-st}\left\{\int_0^t \exp\left[-\frac{\gamma_{\rm d}^2(t-t')^2}{2}\right]e^{\pm i\omega_0(t-t')}\langle\mathcal{O}(t')\rangle dt'\right\}dt \tag{A10}$$
$$= \int_0^\infty\int_{t'}^\infty \exp\left[-\frac{\gamma_{\rm d}^2(t-t')^2}{2}\right]e^{-st\pm i\omega_0(t-t')}\langle\mathcal{O}(t')\rangle dt dt' \tag{A11}$$
$$= \int_0^\infty\left\{\int_{t'}^\infty \exp\left[-\frac{\gamma_{\rm d}^2(t-t')^2}{2}\right]e^{-(s\mp i\omega_0)(t-t')}dt\right\}e^{-st'}\langle\mathcal{O}(t')\rangle dt' \tag{A12}$$
$$= \int_0^\infty\left[\int_0^\infty \exp\left(-\frac{\gamma_{\rm d}^2\tau^2}{2}\right)e^{-(s\mp i\omega_0)\tau}d\tau\right]e^{-st'}\langle\mathcal{O}(t')\rangle dt' \tag{A13}$$
$$= \frac{1}{\gamma_{\rm d}}\sqrt{\frac{\pi}{2}}\exp(z_\mp^2)\mathrm{erfc}(z_\mp)\langle\tilde{\mathcal{O}}(s)\rangle, \tag{A14}$$

where $z_\pm = (s \pm i\omega_0)/(\gamma_{\rm d}\sqrt{2})$, $\langle\tilde{\mathcal{O}}(s)\rangle$ is the Laplace transform of $\langle\mathcal{O}(t)\rangle$, and $\mathrm{erfc}(z)$ is the complementary error function. The Laplace transform of Eq. (A6) then gives

$$(s+\kappa+i\omega)\langle\tilde a(s)\rangle - a(0) = -\frac{\lambda_r^2}{\gamma_{\rm d}}\sqrt{\frac{\pi}{2}}f(z_+)\langle\tilde a(s)\rangle + \frac{\lambda_s^2}{\gamma_{\rm d}}\sqrt{\frac{\pi}{2}}f(z_-)\langle\tilde a(s)\rangle$$
$$- \frac{\lambda_r\lambda_s}{\gamma_{\rm d}}\sqrt{\frac{\pi}{2}}f(z_+)\langle\tilde a^\dagger(s)\rangle + \frac{\lambda_r\lambda_s}{\gamma_{\rm d}}\sqrt{\frac{\pi}{2}}f(z_-)\langle\tilde a^\dagger(s)\rangle, \tag{A15}$$

where $f(z) = e^{z^2}\mathrm{erfc}(z)$ and $\lambda_r\lambda_s$ is set to zero in the copropagating case. It is convenient to scale $s,\kappa,\omega,\omega_0,\lambda_{r,s}$, and $a(0)$ by the factor $\gamma_{\rm d}\sqrt{2}$ to give the scaled form,

$$(z+\bar\kappa+i\bar\omega)\langle\tilde a(z)\rangle - \bar a(0) = -\left[\bar\lambda_r^2 f(z_+) - \bar\lambda_s^2 f(z_-)\right]\sqrt{\pi}\langle\tilde a(z)\rangle - \bar\lambda_r\bar\lambda_s\sqrt{\pi}[f(z_+) - f(z_-)]\langle\tilde a^\dagger(z)\rangle. \tag{A16}$$

If any of the poles of $\langle\tilde a(z)\rangle$ have a positive real part, the solution describes an amplification process, that is, a growth of the cavity field and transfer of atomic population. The threshold is then determined by the smallest value of $\bar\lambda$ at which a pole crosses the imaginary axis.

For the single-beam case ($\bar\lambda_r = 0$), the Laplace transform solution is

$$\langle\tilde a(z)\rangle = \frac{\bar a(0)}{z_- + z_0 - \bar\lambda^2\sqrt{\pi}f(z_-)}, \tag{A17}$$

where $z_0 = \bar\kappa + i(\bar\omega + \bar\omega_0) = \bar\kappa - i\bar\delta_{\rm cs}$. Since z_- is simply a translation of z along the imaginary axis, the threshold is also indicated by poles in the positive half space of the z_- plane. The threshold can be found by the requirement that the denominator of $\langle\tilde a(z)\rangle$

is zero for $z_- = iy$. This gives $\bar{\lambda}^2 = \bar{\kappa} e^{y^2}/\sqrt{\pi}$, where y satisfies

$$\bar{\delta}_{\rm cs} = y + \frac{2\bar{\kappa}}{\sqrt{\pi}} e^{y^2} F(y), \tag{A18}$$

in which $F(y)$ is the Dawson function defined by

$$F(y) = e^{-y^2} \int_0^y e^{x^2} dx. \tag{A19}$$

For $\bar{\delta}_{\rm cs} = 0$, $y = 0$, giving the resonant threshold $\bar{\lambda}^2 = \bar{\kappa}/\sqrt{\pi}$. All other values can be found numerically.

In the copropagating case ($\bar{\lambda}_r = \bar{\lambda}_s = \bar{\lambda}, \bar{\lambda}_r \bar{\lambda}_s \to 0$), the Laplace transform is

$$\langle \tilde{a}(z) \rangle = \frac{\bar{a}(0)}{z + \bar{\kappa} + i\bar{\omega} + \bar{\lambda}^2 \sqrt{\pi}[f(z_+) - f(z_-)]}. \tag{A20}$$

In the special case $\omega_0 = 0$, $z_+ = z_-$ and there is no dependence on $\bar{\lambda}$. Consequently, no threshold exists. For other values, the threshold can be found numerically.

In the counterpropagating case, $\bar{\lambda}_s = \bar{\lambda}_r = \bar{\lambda}$ and the Laplace transform is

$$(z + \bar{\kappa} + i\bar{\omega})\langle \tilde{a}(z) \rangle - \bar{a}(0) = \bar{\lambda}^2 \sqrt{\pi}[f(z_-) - f(z_+)][\langle \tilde{a}(z) \rangle + \langle \tilde{a}^\dagger(z) \rangle], \tag{A21}$$

with the corresponding equation for $\langle \tilde{a}^\dagger(z) \rangle$,

$$(z + \bar{\kappa} - i\bar{\omega})\langle \tilde{a}^\dagger(z) \rangle - \bar{a}^\dagger(0) = -\bar{\lambda}^2 \sqrt{\pi}[f(z_-) - f(z_+)][\langle \tilde{a}(z) \rangle + \langle \tilde{a}^\dagger(z) \rangle]. \tag{A22}$$

These two equations may be expressed in matrix form,

$$\begin{pmatrix} z + \bar{\kappa} + i\bar{\omega} - \bar{\lambda}^2 \sqrt{\pi}[f(z_-) - f(z_+)] & -\bar{\lambda}^2 \sqrt{\pi}[f(z_-) - f(z_+)] \\ \bar{\lambda}^2 \sqrt{\pi}[f(z_-) - f(z_+)] & z + \bar{\kappa} - i\bar{\omega} + \bar{\lambda}^2 \sqrt{\pi}[f(z_-) - f(z_+)] \end{pmatrix} \begin{pmatrix} \tilde{a}(z) \rangle \\ \tilde{a}^\dagger(z) \rangle \end{pmatrix} = \begin{pmatrix} \bar{a}(0) \\ \bar{a}^\dagger(0) \end{pmatrix}. \tag{A23}$$

Poles in $\langle \tilde{a}(z) \rangle$ are then roots of the determinant,

$$(z + \bar{\kappa})^2 + \bar{\omega}^2 + 2i\bar{\omega}\bar{\lambda}^2 \sqrt{\pi}[f(z_-) - f(z_+)]. \tag{A24}$$

When $\omega\omega_0 < 0$, the threshold can be found numerically. When $\omega\omega_0 \geqslant 0$, roots of this expression first cross into the positive half space of the z plane along the real axis. Hence, we can set $z = 0$ and solve for $\bar{\lambda}$. This gives the expression

$$\bar{\lambda} = \sqrt{\frac{\bar{\omega}^2 + \bar{\kappa}^2}{8\bar{\omega} F(\bar{\omega}_0)}}. \tag{A25}$$

Since we are considering behavior below threshold, the nonlinear term $(\delta a^\dagger a J_z/N)$ in Eq. (13) simply adds a small detuning $(-\delta/2)$ to ω.

[1] R. H. Dicke, Coherence in spontaneous radiation processes, Phys. Rev. **93**, 99 (1954).

[2] F. Dimer, B. Estienne, A. S. Parkins, and H. J. Carmichael, Proposed realization of the Dicke-model quantum phase transition in an optical cavity QED system, Phys. Rev. A **75**, 013804 (2007).

[3] K. Hepp, and E. H. Lieb, On the superradiant phase transition for molecules in a quantized radiation field: The Dicke master model, Ann. Phys. **76**, 360 (1973).

[4] K. Hepp, and E. H. Lieb, Equilibrium statistical mechanics of matter interacting with the quantized radiation field, Phys. Rev. A **8**, 2517 (1973).

[5] M. J. Bhaseen, J. Mayoh, B. D. Simons, and J. Keeling, Dynamics of nonequilibrium Dicke models, Phys. Rev. A **85**, 013817 (2012).

[6] Z. Zhiqiang, C. H. Lee, R. Kumar, K. J. Arnold, S. J. Masson, A. S. Parkins, and M. D. Barrett, Non-equilibrium phase transition in a spin one Dicke model, Optica **4**, 424 (2017).

[7] K. Baumann, C. Guerlin, F. Brennecke, and T. Esslinger, Dicke quantum phase transition with a superfluid gas in an optical cavity, Nature (London) **464**, 1301 (2010).

[8] V. M. Bastidas, C. Emary, B. Regler, and T. Brandes, Nonequilibrium Quantum Phase Transitions in the Dicke Model, Phys. Rev. Lett. **108**, 043003 (2012).

[9] P. Kirton and J. Keeling, Suppressing and Restoring the Dicke Superradiance Transition by Dephasing and Decay, Phys. Rev. Lett. **118**, 123602 (2017).

[10] D. Nagy, G. Kónya, G. Szirmai, and P. Domokos, Dicke-Model Phase Transition in the Quantum Motion of a Bose-Einstein Condensate in an Optical Cavity, Phys. Rev. Lett. **104**, 130401 (2010).

[11] T. Niemczyk, F. Deppe, H. Huebl, E. P. Menzel, F. Hocke, M. J. Schwarz, J. J. Garcia-Ripoll, D. Zueco, T. Hümmer, E. Solano *et al.*, Circuit quantum electrodynamics in the ultrastrong-coupling regime, Nat. Phys. **6**, 772 (2010).

[12] O. Viehmann, J. von Delft, and F. Marquardt, Superradiant Phase Transitions and the Standard Description of Circuit QED, Phys. Rev. Lett. **107**, 113602 (2011).

[13] Y. Zhang, L. Yu, J.-Q. Liang, G. Chen, S. Jia, and F. Nori, Quantum phases in circuit QED with a superconducting qubit array, Sci. Rep. **4**, 4083 (2014).

[14] H. Zhu, G. Zhang, and H. Fan, Quantum criticality in the biased Dicke model, Sci. Rep. **6**, 19751 (2016).
[15] J. A. Mlynek, A. A. Abdumalikov, C. Eichler, and A. Wallraff, Observation of Dicke superradiance for two artificial atoms in a cavity with high decay rate, Nat. Commun. **5**, 5186 (2014).
[16] Y. K. Wang and F. T. Hioe, Phase transition in the Dicke model of superradiance, Phys. Rev. A **7**, 831 (1973).
[17] J. Larson, and M. Lewenstein, Dilute gas of ultracold two-level atoms inside a cavity: Generalized Dicke model, New J. Phys. **11**, 063027 (2009).
[18] M. Hayn, and T. Brandes, Thermodynamics and superradiant phase transitions in a three-level Dicke model, Phys. Rev. E **95**, 012153 (2017).
[19] C. Emary, and T. Brandes, Chaos and the quantum phase transition in the Dicke model, Phys. Rev. E **67**, 066203 (2003).
[20] J. Vidal and S. Dusuel, Finite-size scaling exponents in the Dicke model, Europhys. Lett. **74**, 817 (2006).
[21] G. Kónya, D. Nagy, G. Szirmai, and P. Domokos, Finite-size scaling in the quantum phase transition of the open-system Dicke model, Phys. Rev. A **86**, 013641 (2012).
[22] J. Keeling, M. J. Bhaseen, and B. D. Simons, Collective Dynamics of Bose-Einstein Condensates in Optical Cavities, Phys. Rev. Lett. **105**, 043001 (2010).
[23] D. Nagy, G. Szirmai, and P. Domokos, Critical exponent of a quantum-noise-driven phase transition: The open-system Dicke model, Phys. Rev. A **84**, 043637 (2011).
[24] B. Öztop, M. Bordyuh, O. E. Müstecaplıoğlu, and H. E. Türeci, Excitations of optically driven atomic condensate in a cavity: Theory of photodetection measurements, New J. Phys. **14**, 085011 (2012).
[25] J. G. Bohnet, Z. Chen, J. M. Weiner, K. C. Cox, and J. K. Thompson, Relaxation Oscillations, Stability, and Cavity Feedback in a Superradiant Raman Laser, Phys. Rev. Lett. **109**, 253602 (2012).
[26] E. G. D. Torre, S. Diehl, M. D. Lukin, S. Sachdev, and P. Strack, Keldysh approach for nonequilibrium phase transitions in quantum optics: Beyond the Dicke model in optical cavities, Phys. Rev. A **87**, 023831 (2013).
[27] W. Kopylov, C. Emary, and T. Brandes, Counting statistics of the Dicke superradiance phase transition, Phys. Rev. A **87**, 043840 (2013).
[28] S. Genway, W. Li, C. Ates, B. P. Lanyon, and I. Lesanovsky, Generalized Dicke Nonequilibrium Dynamics in Trapped Ions, Phys. Rev. Lett. **112**, 023603 (2014).
[29] E. G. Dalla Torre, Y. Shchadilova, E. Y. Wilner, M. D. Lukin, and E. Demler, Dicke phase transition without total spin conservation, Phys. Rev. A **94**, 061802 (2016).
[30] J. Gelhausen, M. Buchhold, and P. Strack, Many-body quantum optics with decaying atomic spin states: (γ, κ) Dicke model, Phys. Rev. A **95**, 063824 (2017).
[31] P. Strack and S. Sachdev, Dicke Quantum Spin Glass of Atoms and Photons, Phys. Rev. Lett. **107**, 277202 (2011).
[32] L. Song, D. Yan, J. Ma, and X. Wang, Spin squeezing as an indicator of quantum chaos in the Dicke model, Phys. Rev. E **79**, 046220 (2009).
[33] S. J. Masson, M. D. Barrett, and A. S. Parkins, Cavity QED Engineering of Spin Dynamics and Squeezing in a Spinor Gas, Phys. Rev. Lett. **119**, 213601 (2017).
[34] K. Baumann, R. Mottl, F. Brennecke, and T. Esslinger, Exploring Symmetry Breaking at the Dicke Quantum Phase Transition, Phys. Rev. Lett. **107**, 140402 (2011).
[35] R. Mottl, F. Brennecke, K. Baumann, R. Landig, T. Donner, and T. Esslinger, Roton-type mode softening in a quantum gas with cavity-mediated long-range interactions, Science **336**, 1570 (2012).
[36] F. Brennecke, R. Mottl, K. Baumann, R. Landig, T. Donner, and T. Esslinger, Real-time observation of fluctuations at the driven-dissipative Dicke phase transition, Proc. Natl. Acad. Sci. USA **110**, 11763 (2013).
[37] D. Schmidt, H. Tomczyk, S. Slama, and C. Zimmermann, Dynamical Instability of a Bose-Einstein Condensate in an Optical Ring Resonator, Phys. Rev. Lett. **112**, 115302 (2014).
[38] J. Klinder, H. Keßler, M. Wolke, L. Mathey, and A. Hemmerich, Dynamical phase transition in the open Dicke model, Proc. Natl. Acad. Sci. USA **112**, 3290 (2015).
[39] M. P. Baden, K. J. Arnold, A. L. Grimsmo, S. Parkins, and M. D. Barrett, Realization of the Dicke Model Using Cavity-Assisted Raman Transitions, Phys. Rev. Lett. **113**, 020408 (2014); **118**, 199901(E) (2017).
[40] K. J. Arnold, M. P. Baden, and M. D. Barrett, Self-Organization Threshold Scaling for Thermal Atoms Coupled to a Cavity, Phys. Rev. Lett. **109**, 153002 (2012).
[41] Strictly speaking, ω_0 is not fixed as it depends on the differential dispersive shift. However, this only changes the value of ω_0 by $\sim$10 kHz for the range of parameters explored.